

NRC Publications Archive Archives des publications du CNRC

Star formation at the epoch of reionization with CANUCS: the ages of stellar populations in MACS1149-JD1

Bradač, Maruša; Strait, Victoria; Mowla, Lamiya; Iyer, Kartheik G.; Noirot, Gaël; Willott, Chris; Brammer, Gabe; Abraham, Roberto; Asada, Yoshihisa; Desprez, Guillaume; Estrada-Carpenter, Vince; Harshan, Anishya; Martis, Nicholas S.; Matharu, Jasleen; Muzzin, Adam; Rihtaršič, Gregor; Sarrouh, Ghassan T. E.; Sawicki, Marcin

This publication could be one of several versions: author's original, accepted manuscript or the publisher's version. / La version de cette publication peut être l'une des suivantes : la version prépublication de l'auteur, la version acceptée du manuscrit ou la version de l'éditeur.

For the publisher's version, please access the DOI link below. / Pour consulter la version de l'éditeur, utilisez le lien DOI ci-dessous.

Publisher's version / Version de l'éditeur:

<https://doi.org/10.3847/2041-8213/ad0e73>

The Astrophysical Journal Letters, 961, 1, pp. 1-7, 2024-01-20

NRC Publications Archive Record / Notice des Archives des publications du CNRC :

<https://nrc-publications.canada.ca/eng/view/object/?id=6228169e-2a34-4273-b74b-55bae948f057>

<https://publications-cnrc.canada.ca/fra/voir/objet/?id=6228169e-2a34-4273-b74b-55bae948f057>

Access and use of this website and the material on it are subject to the Terms and Conditions set forth at

<https://nrc-publications.canada.ca/eng/copyright>

READ THESE TERMS AND CONDITIONS CAREFULLY BEFORE USING THIS WEBSITE.

L'accès à ce site Web et l'utilisation de son contenu sont assujettis aux conditions présentées dans le site

<https://publications-cnrc.canada.ca/fra/droits>

LISEZ CES CONDITIONS ATTENTIVEMENT AVANT D'UTILISER CE SITE WEB.

Questions? Contact the NRC Publications Archive team at

PublicationsArchive-ArchivesPublications@nrc-cnrc.gc.ca. If you wish to email the authors directly, please see the first page of the publication for their contact information.

Vous avez des questions? Nous pouvons vous aider. Pour communiquer directement avec un auteur, consultez la première page de la revue dans laquelle son article a été publié afin de trouver ses coordonnées. Si vous n'arrivez pas à les repérer, communiquez avec nous à PublicationsArchive-ArchivesPublications@nrc-cnrc.gc.ca.



Star Formation at the Epoch of Reionization with CANUCS: The Ages of Stellar Populations in MACS1149-JD1

Maruša Bradač^{1,2} , Victoria Strait^{3,4} , Lamiya Mowla^{5,6} , Kartheik G. Iyer⁶ , Gaël Noirot⁷, Chris Willott⁸ , Gabe Brammer^{3,4} , Roberto Abraham⁹ , Yoshihisa Asada^{7,10} , Guillaume Desprez⁷ , Vince Estrada-Carpenter⁷, Anishya Harshan¹ , Nicholas S. Martis^{1,7,11} , Jasleen Matharu^{3,4} , Adam Muzzin¹², Gregor Rihtaršič¹ , Ghassan T. E. Sarrouh¹² , and Marcin Sawicki⁷

¹ University of Ljubljana, Department of Mathematics and Physics, Jadranska ulica 19, SI-1000 Ljubljana, Slovenia

² Department of Physics and Astronomy, University of California Davis, 1 Shields Avenue, Davis, CA 95616, USA

³ Cosmic Dawn Center (DAWN), Denmark

⁴ Niels Bohr Institute, University of Copenhagen, Jagtvej 128, DK-2200 Copenhagen N, Denmark

⁵ Whittin Observatory, Department of Physics and Astronomy, Wellesley College, 106 Central Street, Wellesley, MA 02481, USA

⁶ Dunlap Institute for Astronomy and Astrophysics, 50 St. George Street, Toronto, Ontario, M5S 3H4, Canada

⁷ Department of Astronomy and Physics and Institute for Computational Astrophysics, Saint Mary's University, 923 Robie Street, Halifax, Nova Scotia, B3H 3C3, Canada

⁸ NRC Herzberg, 5071 West Saanich Road, Victoria, BC V9E 2E7, Canada

⁹ David A. Dunlap Department of Astronomy and Astrophysics, University of Toronto, 50 St. George Street, Toronto, Ontario M5S 3H4, Canada

¹⁰ Department of Astronomy, Kyoto University, Sakyo-ku, Kyoto 606-8502, Japan

¹¹ National Research Council of Canada, Herzberg Astronomy & Astrophysics Research Centre, 5071 West Saanich Road, Victoria, BC V9E 2E7, Canada

¹² Department of Physics and Astronomy, York University, 4700 Keele Street, Toronto, Ontario, M3J 1P3, Canada

Received 2023 August 24; revised 2023 November 14; accepted 2023 November 21; published 2024 January 17

Abstract

We present measurements of stellar populations properties of a $z = 9.1$ gravitationally lensed galaxy MACS1149-JD1 using deep James Webb Space Telescope NIRISS slitless spectroscopy as well as NIRISS and NIRCам imaging from the CANADIAN NIRISS Unbiased Cluster Survey (CANUCS). The galaxy is split into four components. Three magnified ($\mu \sim 11$) star-forming components are unresolved, giving intrinsic sizes of < 25 pc. In addition, the underlying extended component contains the bulk of the stellar mass, formed the majority of its stars ~ 50 Myr earlier than the other three components, and is not the site of the most active star formation currently. The NIRISS and NIRCам resolved photometry does not confirm a strong Balmer break previously seen in Spitzer. The NIRISS grism spectrum has been extracted for the entire galaxy and shows a clear continuum and Lyman break, with no Ly α detected.

Unified Astronomy Thesaurus concepts: [High-redshift galaxies \(734\)](#); [Gravitational lensing \(670\)](#); [Reionization \(1383\)](#)

1. Introduction

Tracing star formation to the earliest times has been a long-standing goal of extragalactic astronomy. In particular, studying the onset of star formation is of importance not only for galaxy formation models but also for studies of the early universe. Spitzer and the Hubble Space Telescope (HST) played a unique role in determining the onset of star formation of galaxies at redshift $z \gtrsim 6$ (e.g., Bradač 2020 for a review).

The James Webb Space Telescope (JWST; Gardner et al. 2023) is revolutionizing studies of the early onset of star formation in high-redshift galaxies. With the expanded sensitivity, filter set, and wavelength coverage compared to Spitzer, JWST can trace the full spectral energy distribution (SED), and in some cases distinguish strong line emission from breaks due to evolved stars (e.g., Laporte et al. 2023). Early results from JWST appear to show a higher than expected ultraviolet luminosity density at $z > 10$ (Donnan et al. 2023; Harikane et al. 2023). There have also been claims for the presence at $7 < z < 9$ of massive galaxies with strong Balmer breaks in the CEERS survey (Boylan-Kolchin 2023; Labbé

et al. 2023; Lovell et al. 2023). However, studies from other JWST surveys with comparable or larger volumes such as JADES, EPOCHS, and CANADIAN NIRISS Unbiased Cluster Survey (CANUCS) do not find such a high density of massive galaxies with strong Balmer breaks at these redshifts (e.g., Desprez et al. 2023; Endsley et al. 2023b; Trussler et al. 2024).

One of the most intriguing objects showing a potential Balmer break from previous HST and Spitzer studies is the $z = 9.1$ galaxy MACS1149-JD1 behind the cluster MACSJ1149.5+2223. MACS1149-JD1 was originally discovered in HST and shallow Spitzer data in Zheng et al. (2012). It was later detected in both channel 1 and channel 2 Spitzer bands using deeper data (Bradač et al. 2014; Huang et al. 2016; Zheng et al. 2017; Hoag et al. 2018) and its redshift was spectroscopically measured with the [O III]88 μ m line using the Atacama Large Millimeter/submillimeter Array (ALMA) by Hashimoto et al. (2018, hereafter H18). The VLT X-SHOOTER observations also reveal a tentative Ly α emission line, albeit blueshifted with respect to [O III] 88 μ m (H18).

With early data, it was concluded that the nebular emission lines are redshifted out of both Spitzer bands (at $z > 9$), yet the galaxy showed a strong color excess. It was therefore highly likely that old (~ 300 Myr) stellar populations are causing the red rest-frame optical colors (H18; Huang et al. 2016; Hoag

et al. 2018). This was surprising, given the galaxy would need to start forming a significant amount of stars shortly after the Big Bang (~ 250 Myr). In addition, the cold dust content of the galaxy was constrained to be modest from observations taken with ALMA, making dust an unlikely cause of red Spitzer color (H18).

MACS1149-JD1 was recently observed as part of the CANUCS (Willott et al. 2022) with the NIRCcam and NIRISS instruments on board JWST. The data provide superior depth, resolution, and wavelength coverage compared to what was possible with Spitzer. In addition, NIRISS spectra with its coverage from 1 to $2.5 \mu\text{m}$ allow us to investigate the rest-frame UV spectrum, including searching for the presence of potential Ly α line (previously mentioned in H18). Here we describe these data and analysis of the stellar properties of MACS1149-JD1. We also note that after the submission of this paper, two further papers with complementary NIRSpec (Stiavelli et al. 2023) and MIRI observations (Álvarez-Márquez et al. 2023) have been submitted. We also briefly discuss those results.

The paper is structured as follows. In Section 2 we present the data used in this paper and in Section 3 we describe the analysis of the photometric and spectroscopic data. In Section 4 we present the main science results. We summarize in Section 5 and give photometry and SED fitting results in the tables in the Appendix. Throughout the paper we assume Λ CDM cosmology with $\Omega_m = 0.3$ and Hubble constant $H_0 = 70 \text{ km s}^{-1} \text{ Mpc}^{-1}$ for the ease of comparison with previous work.

2. Data

JWST NIRISS, and NIRCcam observations of MACS1149-JD1 were taken from 2023 May 10 to 22 as part of the NIRISS GTO Program #1208, CANUCS (Willott et al. 2022; doi:10.17909/ph4n-6n76).

The field was observed with NIRCcam imaging using filters F090W, F115W, F150W, F200W, F277W, F356W, F410M, and F444W with exposure times of 6.4 ks each, reaching a signal-to-noise ratio (S/N) between 5 and 10 for a $m_{\text{AB}} = 29$ point source. We also utilized archival data of HST imaging from Hubble Frontier Fields (HFF; Lotz et al. 2017), GLASS (Treu et al. 2015), and SN Refsdal (Kelly et al. 2015) follow-up observations (HST-GO-13504, PI Lotz; HST-GO-13790, PI Rodney; HST-GO-13459, PI Treu; HST-GO-14041, PI Kelly).

To reduce the imaging data, we use the photometric pipeline that is presented in more detail in Asada et al. (2024). Briefly, the raw data have been reduced using the public Grism redshift and line analysis software Grizli (Brammer 2023), which masks imaging artifacts, provides astrometric calibrations based on the Gaia Data Release 3 catalog, and shifts images using Astrodizzle. The photometric zero-points are applied as described in Brammer (2022). We show the cutouts of MACS1149-JD1 in Figure 1.

Observations also consist of two NIRISS pointings, one centered on the cluster center containing MACS1149-JD1 and the other coincident with a flanking field. Each pointing is observed with the GR150R and GR150C grisms through the F115W, F150W, and F200W filters. Exposure times for the cluster field are 19,240 s in each of the three filters. We also process all the NIRISS imaging and slitless spectroscopy with Grizli, using calibrations described in Matharu & Brammer (2022). Grizli performs full end-to-end processing of space-

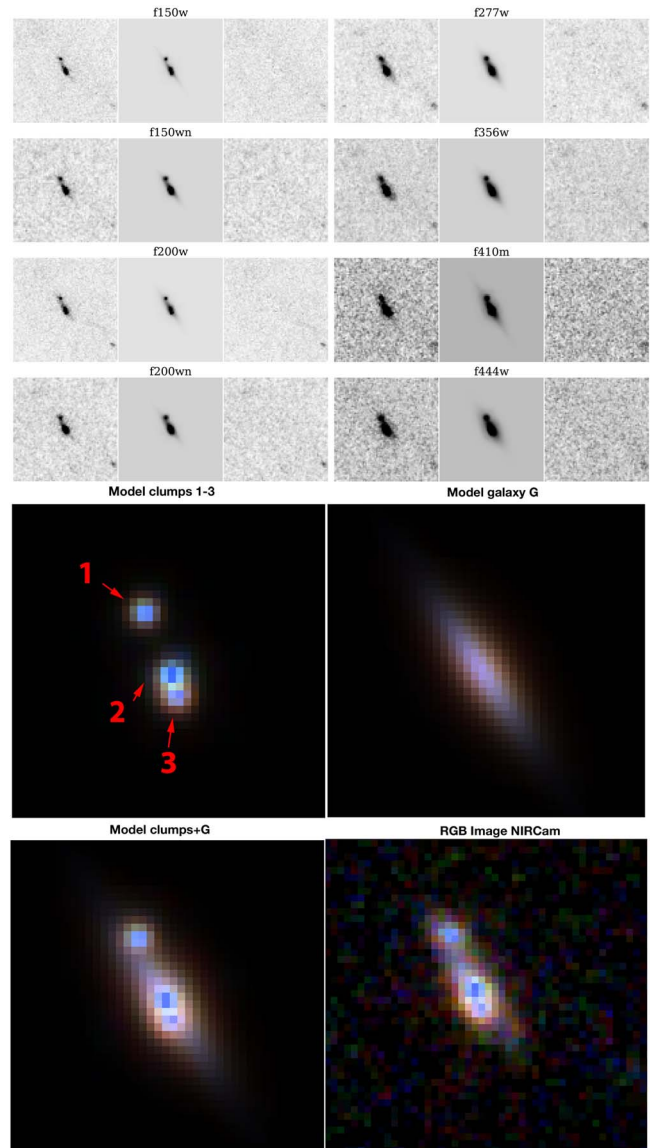


Figure 1. Images of the three clumps and underlying galaxy component in MACS1149-JD1. Shown are different filters, Galfit models and residuals (top panels), RGB (always using F150W, F277W, and F444W filters) model of the clumps and the galaxy (middle panels) and RGB model and RGB NIRCcam image (bottom panels). The galaxy consists of at least three clumps (all marked in the middle panel), all of which are unresolved and an underlying smooth component. An upper limit to the magnified size of the clumps is $0''.025$. The intrinsic (demagnified) size upper limit is <25 pc.

based slitless spectroscopic data sets. For full details see, e.g., Matharu et al. (2021, 2023) and Noiro et al. (2023). In summary, raw data are downloaded from the Mikulski Archive for Space Telescopes (MAST) and preprocessed for cosmic rays, flat-fielding, sky subtraction, and astrometric corrections and alignment. Contamination models (which correct for overlapping spectra from nearby sources) for each pointing are then generated and subtracted for each grism spectrum of interest. From these images we extract the spectrum of MACS1149-JD1.

For the magnification estimate, we updated the Lenstool model from Jauzac et al. (2016) and Desprez et al. (2018). We used lensing constraints described in Desprez et al. (2018), updated with new NIRISS spectroscopic data. We measured spectroscopic redshifts of four systems, bringing the total

Table 1
JWST Photometry (Fluxes for All Four Components) of MACS1149-JD1

Filter	C #1 (nJy)	C #2 (nJy)	C #3 (nJy)	G (nJy)
NIRISS				
F150W	28 ± 3	45 ± 3	29 ± 3	125 ± 10
F200W	30 ± 3	42 ± 5	27 ± 4	113 ± 12
NIRCam				
F150W	32 ± 2	55 ± 3	34 ± 3	112 ± 14
F200W	26 ± 2	47 ± 2	27 ± 2	133 ± 12
F277W	23 ± 2	34 ± 4	24 ± 4	121 ± 17
F356W	17 ± 2	33 ± 6	22 ± 5	133 ± 18
F410M	22 ± 2	23 ± 7	18 ± 6	152 ± 19
F444W	25 ± 3	25 ± 12	33 ± 9	163 ± 25

number of spectroscopically confirmed systems to 12. With high-resolution NIRCam imaging, we also identified new multiply imaged clumps in five known systems. Full details will be described in an upcoming paper (G. Rihtaršič et al. 2024, in preparation). The corresponding magnification is $\mu_{\text{best}} = 11_{-4}^{+1}$ (68% confidence). It is in agreement with the median magnification $\mu_{\text{models}} = 17_{-12}^{+140}$ from the seven other publicly available post-HFF lens models (Bradacv4 $\mu = 17_{-5}^{+3}$, CATSv4.1 $\mu = 160_{-10}^{+120}$, Sharonv4cor $\mu = 6.5 \pm 0.5$, Keetonv4 $\mu = 8_{-2}^{+4}$, Williamsv4 $\mu = 30_{-26}^{+1}$, Diegov4.1 $\mu = 5.0_{-1.0}^{+0.1}$, GLAFICv3 $\mu = 17_{-13}^{+10}$) published on MAST.¹³ Throughout the paper we correct for gravitational lensing magnification μ_{best} all properties as appropriate unless otherwise noted.

3. Data Analysis

3.1. Photometry and SED Fitting

The photometry is derived using the updated zero-points (Brammer 2022), and corrected for Milky Way extinction using the value of color excess $E(B - V) = 0.0272$ from Schlafly & Finkbeiner (2011) and assuming the extinction law by Fitzpatrick (1999) using the factor between the extinction coefficient and color excess $R_V = 3.1$. We use F150W and F200W NIRISS filters as well as F150W, F200W, F277W, F356W, F410M, and F444W NIRCam filters (in other JWST filters MACS1149-JD1 is not/barely detected) and HST upper limits for the entire source. Since the object is resolved into three distinct clumps and a smooth galaxy component, we perform a photometric fit using Galfit (Peng et al. 2010). We measure empirical point-spread function (PSF) determined from the observations of stars. We fit point sources for the three clumps and a Sérsic profile for the smooth galaxy component, convolved by the respective filter PSF, in every filter image where the galaxy is detected. We provide an initial guess for the coordinates of the four components allowing them to vary by ± 0.2 pixel ($0''.08$) in each direction to account for the centroiding error of the empirical PSF in each filter. The total flux for each of the four components are determined by Galfit by minimizing the residuals (Table 1). The effective (lensed) radius and Sérsic index of the smooth component is $0''.30 \pm 0''.02$ and 1.0 ± 0.2 , respectively. We correct the smooth component size using total magnification ($\sqrt{\mu}$) and

obtain intrinsic size of $R_e = 560_{-50}^{+150}$ pc. The clumps are unresolved even in our highest-resolution F150W NIRISS image. We use the half-width at half-maximum of the F150W PSF ($0''.025$) to set an upper limit on size of the clumps. To determine the upper limits of the sizes of unresolved sources, we use tangential eigenvalue of magnification $1/|\lambda_t|$ and determine the limit of < 25 pc (Table 2).

The resulting models and residuals are shown in Figure 1. Residuals from the fits are negligible, confirming the original visual impression that the three compact sources are unresolved and an additional smooth component is present. The agreement between NIRISS and NIRCam fluxes in the two overlapping filters is a confirmation of the robustness of photometry. Resolved photometry is necessary, as global SED fitting can bias stellar masses when young stellar population outshine the first episodes of star formation (e.g., Sorba & Sawicki 2018; Giménez-Arteaga et al. 2023; Narayanan et al. 2023). Photometric properties are given in Table 1.

SEDs derived from our photometry were analyzed using the DENSE BASIS method (Iyer & Gawiser 2017; Iyer et al. 2019) to determine nonparametric star formation histories (SFHs), masses, and ages for our sources in MACS1149-JD1. We adopt the Calzetti attenuation law (Calzetti 2001) and a Chabrier initial mass function (Chabrier 2003). We fix the redshift to that found by the [O III]88 μm line in H18, 9.1096 ± 0.0006 . All other parameters are left free. The primary advantage of using DENSE BASIS with nonparametric SFHs is that they allow us to account for flexible stellar populations. Both photometry and SED fit are shown in Figure 2.

3.2. Grism Spectroscopy

To extract the NIRISS spectrum of the source, we also use the Grizli package. The Grizli reduction steps of the NIRISS data include the creation of an NIRISS direct image mosaic from which diffraction spikes of bright sources are masked. Following Noirot et al. (2023), source detection is performed on the NIRISS mosaic image with the Source Extractor (Bertin & Arnouts 1996) python wrapper sep (Barbary 2016), using the default detection parameters implemented in Grizli (a detection threshold “threshold” of 1.8σ above the global background rms, a minimum source area in pixels “minarea” of 9, and deblending parameters “deblend_cont” and “deblend_ntresh” of 0.001 and 32, respectively). Matched aperture photometry on the available NIRISS filters is performed at the same stage. From this NIRISS imaging catalog, the positions of sources that contaminate the spectrum of MACS1149-JD1 are used to locate spectral traces in the grism data. The spectral continua of the sources are modeled using an iterative polynomial fitting of the data for contamination estimate and removal. The 2D and extracted 1D MACS1149-JD1 spectra with contamination removal and modeled spectrum are shown in Figure 3.

4. Results

4.1. Spatially Resolved Star Formation History

Using our photometry (Table 1), we now determine the stellar properties of each individual component. By determining β_{UV} slopes based on NIRCam F150W, F200W, and F227W fluxes, we see that the three clumps have different properties than the underlying galaxy component. The three clumps have $\beta_{\text{UV,phot}}$ measured between -2.5 and -2.8 ,

¹³ <https://archive.stsci.edu/prepds/frontier/lensmodels/>

Table 2
Global Properties of MACS1149-JD1 and Stellar Properties of Individual Clumps

Parameter	C #1	C #2	C #3	G
R.A. (deg)				177.3899418
Decl. (deg)				22.4126885
z_{spec}^a				9.1096 ± 0.0006
μ_{best}				11_{-4}^{+1}
$1/ \lambda_t $				$7.2_{-2.1}^{+0.6}$
$\beta_{\text{UV,phot}}$	-2.6 ± 0.1	-2.8 ± 0.1	-2.5 ± 0.2	-1.9 ± 0.2
$M^* (M_{\odot})$	$1.0_{-0.6}^{+1.7} \times 10^7$	$1.4_{-0.7}^{+2.3} \times 10^7$	$1.7_{-1.2}^{+5.3} \times 10^7$	$1.5_{-1.1}^{+4.0} \times 10^8$
$\text{SFR} (M_{\odot} \text{ Myr}^{-1})$	$0.30_{-0.17}^{+0.14}$	$0.44_{-0.24}^{+0.20}$	$0.31_{-0.24}^{+0.24}$	$1.5_{-1.3}^{+2.2}$
$t_{50} \text{ (Myr)}$	85_{-69}^{+108}	85_{-69}^{+103}	85_{-68}^{+126}	139_{-84}^{+83}
$R_c \text{ (lensed)}$	$<0''.025$	$<0''.025$	$<0''.025$	$0''.30 \pm 0''.02$
R_c^b	$<25 \text{ pc}$	$<25 \text{ pc}$	$<25 \text{ pc}$	$560_{-50}^{+150} \text{ pc}$

Notes.

^a From H18.

^b The size of G was corrected using $1/\sqrt{\mu_{\text{best}}}$, while the clumps were corrected using $1/|\lambda_t|$.

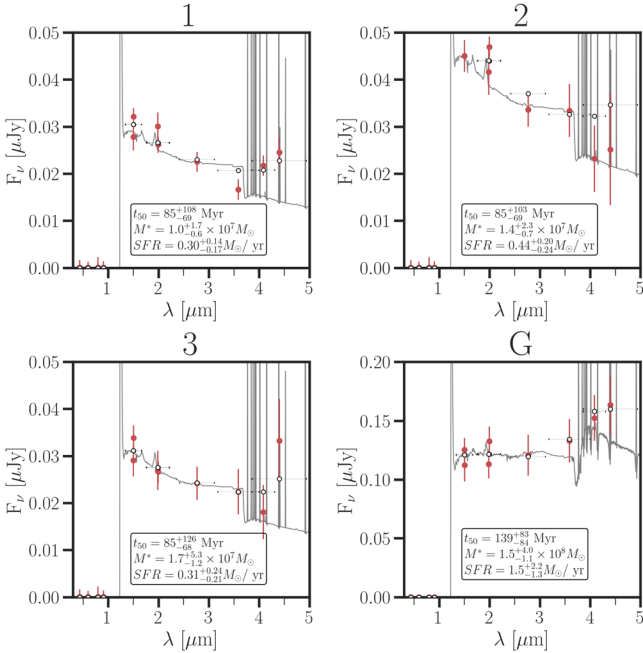


Figure 2. Results of the SED fitting for the three clumps (labeled 1–3) and the smooth light component (G). Shown are measured fluxes (i.e., we do not correct them for magnification) for both NIRCcam and NIRISS imaging in red and SED predicted fluxes in open circles in units of μJy . Derived stellar properties are given in the inset.

whereas the galaxy itself is redder with $\beta_{\text{UV,phot}} = -1.9 \pm 0.2$ (Table 2). The values are consistent with other observations from JWST (e.g., Bouwens et al. 2023; Endsley et al. 2023a; Franco et al. 2023; Topping et al. 2023).

Using DENSE BASIS we also perform the SED fit and determine nonparametric SFHs. All four components have intrinsic (corrected for magnification) stellar masses between 10^7 and $1.5 \times 10^8 M_{\odot}$ and star formation rates (SFR) between 0.3 and $1.5 M_{\odot} \text{ yr}^{-1}$. While the error bars are large and there is still a possibility that all components have the same SFHs, there is nevertheless a hint that the galaxy itself (G) has started to form the bulk of the stars earlier (Figure 4). This component also has the highest stellar mass (Figure 5). In Figure 6 we also show the mass fraction of stars formed as a function of look-

back time. Once again, the error bars are large, but there is an indication that the underlying galaxy has formed the bulk of its stellar masses earlier than the clumps, which are still actively star-forming.

The galaxy formed 50% of its total mass at $t_{50} = 139_{-84}^{+83} \text{ Myr}$. In H18, the bulk of the stellar population was determined to have formed at a look-back time of $\sim 250 \text{ Myr}$. The main reason is that the relative flux measured red-ward of $\sim 4000 \text{ \AA}$ has decreased, making the potential Balmer break less pronounced. We measure the Balmer break of galaxy G (based on fluxes in F444W and F277W, the latter being mostly emission line free) of $\Delta\text{mag}_{\text{AB}} = 0.3 \pm 0.2 \text{ mag}$ ($F_{\nu}(\text{F444W})/F_{\nu}(\text{F277W}) = 1.4 \pm 0.2$). This is lower compared to Spitzer measurements from Kokorev et al. (2022) of $\Delta\text{mag}_{\text{AB}} = 0.5 \pm 0.2$, from Zheng et al. (2017; also used in H18) $\Delta\text{mag}_{\text{AB}} > 1.3 (1\sigma)$, from ASTRODEEP (Di Criscienzo et al. 2017) $\Delta\text{mag}_{\text{AB}} > 0.7 (3\sigma)$, and from (Huang et al. 2016) $\Delta\text{mag}_{\text{AB}} = 0.8 \pm 0.4$. All Spitzer measurements are the average of the older G component and all the clumps, though the former dominates the flux. This discrepancy is unlikely caused by emission lines, as both NIRCcam F444W and Spitzer channel 2 have similar throughputs at the red end, hence entering the [O III] $\lambda 4959$ emission line (where both instruments have a throughput of 20%) could not play a role (for [O III] $\lambda 5007$ both are similarly at 1%). We think the most likely source of discrepancy is the contamination modeling, which in the case of Spitzer’s large PSF is difficult.

4.2. Grism Spectrum

We clearly detect the continuum and Lyman break in the NIRISS spectrum at the expected redshift. In Figure 3 we show 1D spectral extraction with a fitted model at the redshift determined by H18. However, even if we let the redshift be determined by the NIRISS data alone, we still recover the same redshift ($z = 9.2 \pm 0.1$). We have also searched for the Ly α emission line that was indicated in H18 at 12267.4 \AA with an integrated (lensed) flux of $4.3 \pm 1.1 \times 10^{-18} \text{ erg s}^{-1} \text{ cm}^{-2}$. We do not detect any lines at that wavelength. To confirm this, we have injected such a line into the data. If the line is unresolved (as also suggested by the measured FWHM in H18), we would detect it at an S/N of ~ 20 ; a line with twice the resolution of

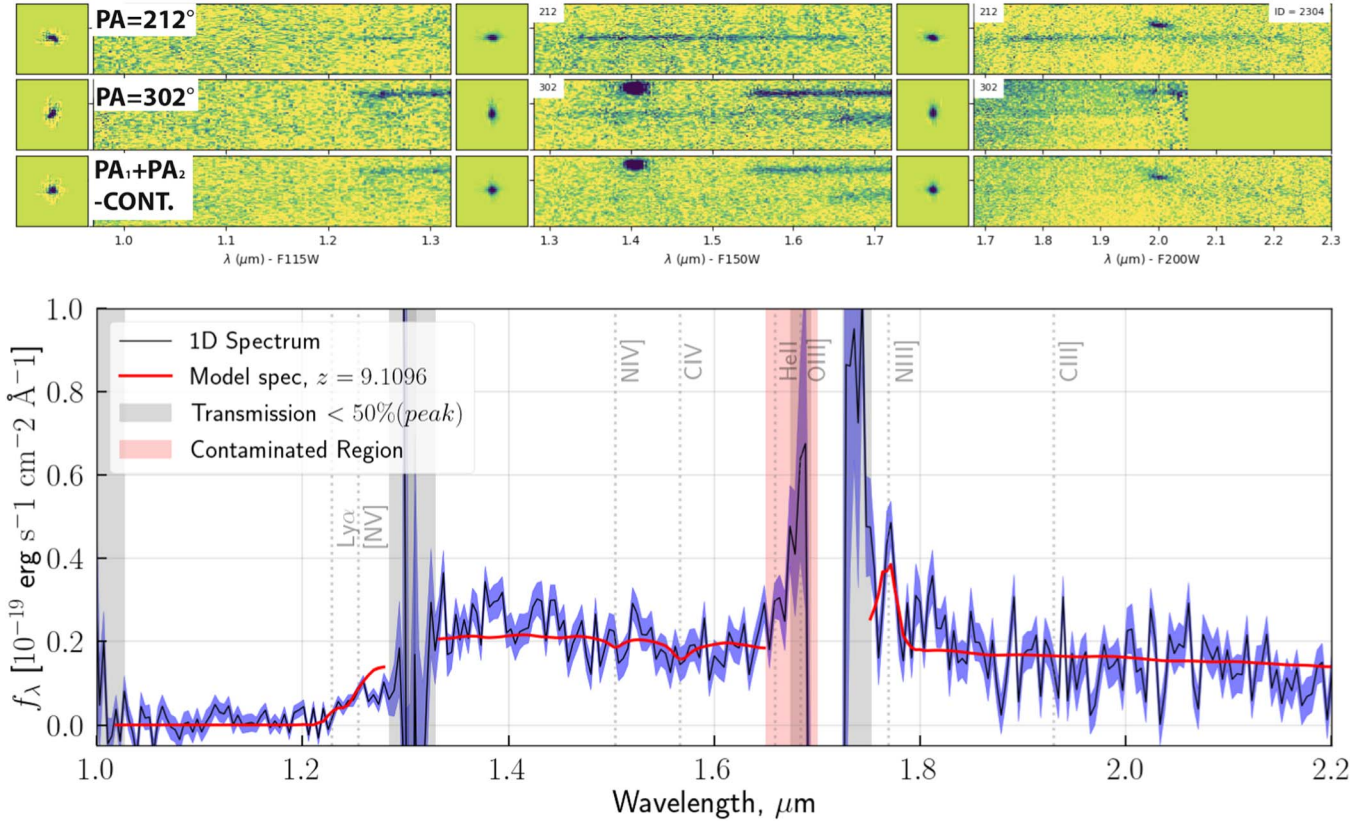


Figure 3. NIRISS grism spectrum of MACS1149-JD1. Top: 2D spectrum of MACS1149-JD1 is shown in two orientations (PA = 212° top and 302° middle) and three filters. Direct images are also shown. The bottom row shows a combined spectrum with continuum emission from the object subtracted. All images are contamination subtracted; the residual contamination is from objects below the imaging detection threshold and objects outside the field of view of the direct imaging. Bottom: 1D spectrum extracted (not corrected for magnification, black line with uncertainties in blue) and modeled given fixed redshift (red line). The positions of potential lines are marked. Only the N III] λ 1747,1749 line is possibly detected in PA = 212°; the other orientation is contaminated and the spectrum falls on the edge of the detector (see top). The region where contamination subtraction failed is marked in red and the region between half power wavelengths at which the transmission in each filter falls below 50% of its peak value is marked in grey.

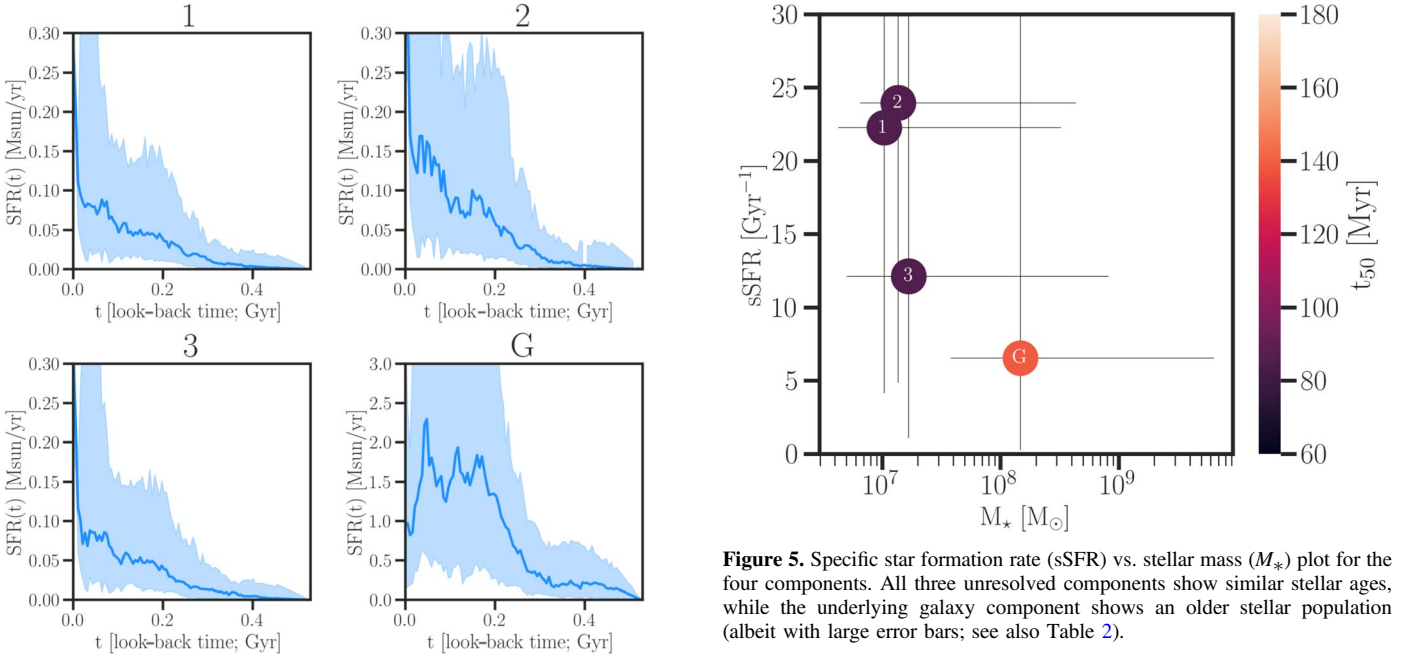


Figure 4. Star formation histories for the four components. While the three star-forming clumps have similar star formation histories, the underlying galaxy component is different.

Figure 5. Specific star formation rate (sSFR) vs. stellar mass (M_*) plot for the four components. All three unresolved components show similar stellar ages, while the underlying galaxy component shows an older stellar population (albeit with large error bars; see also Table 2).

NIRISS at this wavelength would be detected with $S/N \sim 18$. Hence we conclude that, if the flux measurement is correct, such a line would have been detected. We do, however, detect a line of similar flux in one orientation PA = 212° at 17700 \AA ,

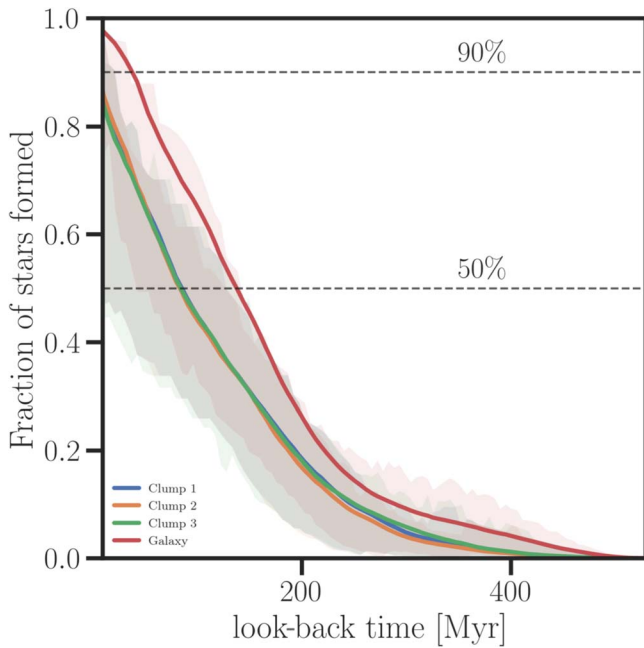


Figure 6. Mass fraction of stars formed as a function of look-back time for all four components (1—blue, 2—orange, 3—green, galaxy—red). In H18 the authors conclude that the bulk of the stellar mass was produced within a short period corresponding to the redshift interval $12 < z < 16$, with a dominant stellar component that formed at the look-back time of ~ 290 Myr. These new measurements show somewhat younger ages, with the oldest component (G) forming 50% of its total mass at $t_{50} = 134^{+89}_{-82}$.

which corresponds to N III] $\lambda 1747, 1749$, with the flux of $4.6 \pm 0.6 \times 10^{-18} \text{ erg s}^{-1} \text{ cm}^{-2}$ and S/N ~ 10 (NIRISS is less sensitive at the blue edge of the F200W filter and the detection is in a single orientation). Unfortunately, the other orientation is contaminated and furthermore, the spectrum is located toward the edge of the detector. Hence, we consider this line tentative.

The combined UV beta slope measured from the NIRISS spectrum between rest-frame wavelengths of 1400–1600 and 1800–2000 Å (we assume a similar spectral range as used for photometry, excluding the part of the spectrum in the detector gap) is $\beta_{\text{UV, spec}} = -2.3 \pm 0.5$. This is consistent with the average photometric measurements done for individual clumps (Table 2).

The spectrum also shows a softening of the Lyman break in the vicinity of $\text{Ly}\alpha$, very likely caused by a largely neutral intergalactic medium (Mason & Gronke 2020; Curtis-Lake et al. 2023; Heintz et al. 2023). Unfortunately, the break falls at the gap between the two filters; hence we cannot characterize it fully.

5. Conclusions

The gravitationally lensed galaxy MACS1149-JD1 at $z = 9.1096 \pm 0.0006$ has been well studied in the past. Spitzer data were showing what seemed to be a strong Balmer break, meaning that the dominant stellar component formed about 290 Myr earlier (or around 240 Myr after the Big Bang; Bradač et al. 2014; Huang et al. 2016; Hoag et al. 2018, H18).

New JWST observations with NIRISS and NIRCам reveal that the galaxy consists of three unresolved (with intrinsic sizes < 25 pc) star-forming clumps and an underlying extended galaxy component. We individually perform SED fitting of all four components (Figure 2, Table 2). The galaxy component

(G) is showing somewhat older stellar population, albeit with large error bars. This component (i) contains the bulk of the stellar mass, (ii) likely formed the majority of its stars ~ 50 Myr earlier than the other components, and (iii) is not the site of the most recent star formation. These findings are consistent with the work of Stiavelli et al. (2023), who, based on the integrated NIRSpec spectrum, conclude that MACS1149-JD1 is indeed a young galaxy. Using MIRI observations, Álvarez-Márquez et al. (2023) report on two clumps (resolution of MIRI is lower than that of the NIRCам) also requiring the presence of very young massive bursts together with older stellar populations.

NIRISS spectrum of MACS1149-JD1 shows a clear detection of the continuum and Lyman break. However, we do not detect the $\text{Ly}\alpha$ line previously reported in H18. Given that NIRISS spectra have low spectral resolution, $\text{Ly}\alpha$ could still be present, though at a lower flux than previously reported.

In conclusion, MACS1149-JD1 is a highly magnified, intrinsically faint galaxy at $z = 9.1$. It shows properties that are consistent with other galaxies detected with JWST (e.g., Bunker et al. 2023; Topping et al. 2023); however, its true nature was only revealed through resolved SED fitting. While strong Balmer breaks can be present at high redshift, they are rare (Endsley et al. 2023b; Laporte et al. 2023; Looser et al. 2023; Strait et al. 2023). With the newest data for MACS1149-JD1, a strong Balmer break is excluded.

Acknowledgments

M.B., G.R., and A.H. acknowledge support from the ERC Grant FIRSTLIGHT and Slovenian national research agency ARRS through grants N1-0238 and P1-0188. M.B. acknowledges support from the program HST-GO-16667, provided through a grant from the STScI under NASA contract NAS5-26555. This research was enabled by grant 18JWST-GTO1 from the Canadian Space Agency and funding from the Natural Sciences and Engineering Research Council of Canada. This research used the Canadian Advanced Network For Astronomy Research (CANFAR) operated in partnership by the Canadian Astronomy Data Centre and The Digital Research Alliance of Canada with support from the National Research Council of Canada the Canadian Space Agency, CANARIE and the Canadian Foundation for Innovation. The Cosmic Dawn Center (DAWN) is funded by the Danish National Research Foundation under grant No. 140. This work utilizes gravitational lensing models produced by PIs Bradač Natarajan & Kneib (CATS), Merten, Zitrin, Sharon, Williams, Keeton, Bernstein and Diego, and the GLAFIC group. This lens modeling was partially funded by the HST Frontier Fields program conducted by STScI. STScI is operated by the Association of Universities for Research in Astronomy, Inc. under NASA contract NAS 5-26555. The lens models were obtained from the Mikulski Archive for Space Telescopes (MAST).

Facilities: HST (ACS, WFC3), JWST (NIRCам, NIRISS).









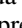
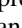
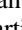


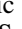

Data Availability

The data are available at doi:[10.17909/ph4n-6n76](https://doi.org/10.17909/ph4n-6n76).

Appendix Photometry and SED Fitting

In Table 1 we list photometry and in Table 2 derived quantities and results of SED fitting of MACS1149-JD1. All the procedures are described in the main text.

ORCID iDs

Maruša Bradač  <https://orcid.org/0000-0001-5984-0395>
 Victoria Strait  <https://orcid.org/0000-0002-6338-7295>
 Lamiya Mowla  <https://orcid.org/0000-0002-8530-9765>
 Kartheik G. Iyer  <https://orcid.org/0000-0001-9298-3523>
 Chris Willott  <https://orcid.org/0000-0002-4201-7367>
 Gabe Brammer  <https://orcid.org/0000-0003-2680-005X>
 Roberto Abraham  <https://orcid.org/0000-0002-4542-921X>
 Yoshihisa Asada  <https://orcid.org/0000-0003-3983-5438>
 Guillaume Desprez  <https://orcid.org/0000-0001-8325-1742>
 Anishya Harshan  <https://orcid.org/0000-0001-9414-6382>
 Nicholas S. Martis  <https://orcid.org/0000-0003-3243-9969>
 Jasleen Matharu  <https://orcid.org/0000-0002-7547-3385>
 Gregor Rihtaršič  <https://orcid.org/0009-0009-4388-898X>
 Ghassan T. E. Sarrouh  <https://orcid.org/0000-0001-8830-2166>
 Marcin Sawicki  <https://orcid.org/0000-0002-7712-7857>

References

- Álvarez-Márquez, J., Colina, L., Crespo Gómez, A., et al. 2023, arXiv:2309.06319
- Asada, Y., Sawicki, M., Abraham, R., et al. 2024, *MNRAS*, 527, 11372
- Barbary, K. 2016, *JOSS*, 1, 58
- Bertin, E., & Arnouts, S. 1996, *A&AS*, 117, 393
- Bouwens, R. J., Stefanon, M., Brammer, G., et al. 2023, *MNRAS*, 523, 1036
- Boylan-Kolchin, M. 2023, *NatAs*, 7, 731
- Bradač, M. 2020, *NatAs*, 4, 478
- Bradač, M., Ryan, R., Casertano, S., et al. 2014, *ApJ*, 785, 108
- Brammer, G. 2022, Preliminary Updates to the NIRCcam Photometric Calibration, v1, Zenodo, doi:10.5281/zenodo.7143382
- Brammer, G. 2023, grizli, v1.9.6, Zenodo, doi:10.5281/zenodo.1146904
- Bunker, A. J., Cameron, A. J., Curtis-Lake, E., et al. 2023, arXiv:2306.02467
- Calzetti, D. 2001, *PASP*, 113, 1449
- Chabrier, G. 2003, *ApJL*, 586, L133
- Curtis-Lake, E., Carniani, S., Cameron, A., et al. 2023, *NatAs*, 7, 622
- Desprez, G., Martis, N. S., Asada, Y., et al. 2023, arXiv:2310.03063
- Desprez, G., Richard, J., Jauzac, M., et al. 2018, *MNRAS*, 479, 2630
- Di Criscienzo, M., Merlin, E., Castellano, M., et al. 2017, *A&A*, 607, A30
- Donnan, C. T., McLeod, D. J., Dunlop, J. S., et al. 2023, *MNRAS*, 518, 6011
- Endsley, R., Stark, D. P., Whitler, L., et al. 2023a, *MNRAS*, 524, 2312
- Endsley, R., Stark, D. P., Whitler, L., et al. 2023b, arXiv:2306.05295
- Fitzpatrick, E. L. 1999, *PASP*, 111, 63
- Franco, M., Akins, H. B., Casey, C. M., et al. 2023, arXiv:2308.00751
- Gardner, J. P., Mather, J. C., Abbott, R., et al. 2023, *PASP*, 135, 068001
- Giménez-Arteaga, C., Oesch, P. A., Brammer, G. B., et al. 2023, *ApJ*, 948, 126
- Harikane, Y., Ouchi, M., Oguri, M., et al. 2023, *ApJS*, 265, 5
- Hashimoto, T., Laporte, N., Mawatari, K., et al. 2018, *Natur*, 557, 392
- Heintz, K. E., Watson, D., Brammer, G., et al. 2023, arXiv:2306.00647
- Hoag, A., Bradač, M., Brammer, G., et al. 2018, *ApJ*, 854, 39
- Huang, K.-H., Lemaux, B. C., Schmidt, K. B., et al. 2016, *ApJL*, 823, L14
- Iyer, K., & Gawiser, E. 2017, *ApJ*, 838, 127
- Iyer, K. G., Gawiser, E., Faber, S. M., et al. 2019, *ApJ*, 879, 116
- Jauzac, M., Richard, J., Limousin, M., et al. 2016, *MNRAS*, 457, 2029
- Kelly, P. L., Rodney, S. A., Treu, T., et al. 2015, *Sci*, 347, 1123
- Kokorev, V., Brammer, G., Fujimoto, S., et al. 2022, *ApJS*, 263, 38
- Labbé, I., van Dokkum, P., Nelson, E., et al. 2023, *Natur*, 616, 266
- Laporte, N., Ellis, R. S., Witten, C. E. C., & Roberts-Borsani, G. 2023, *MNRAS*, 523, 3018
- Looser, T. J., D'Eugenio, F., Maiolino, R., et al. 2023, arXiv:2302.14155
- Lotz, J. M., Koekemoer, A., Coe, D., et al. 2017, *ApJ*, 837, 97
- Lovell, C. C., Harrison, I., Harikane, Y., Tacchella, S., & Wilkins, S. M. 2023, *MNRAS*, 518, 2511
- Mason, C. A., & Gronke, M. 2020, *MNRAS*, 499, 1395
- Matharu, J., & Brammer, G. 2022, Updated Configuration Files for JWST NIRISS Slitless Spectroscopy, v1.0, Zenodo, doi:10.5281/zenodo.7628094
- Matharu, J., Muzzin, A., Brammer, G. B., et al. 2021, *ApJ*, 923, 222
- Matharu, J., Muzzin, A., Sarrouh, G. T. E., et al. 2023, *ApJL*, 949, L11
- Narayanan, D., Lower, S., Torrey, P., et al. 2023, arXiv:2306.10118
- Noirot, G., Desprez, G., Asada, Y., et al. 2023, *MNRAS*, 525, 1867
- Peng, Y.-j., Lilly, S. J., Kovač, K., et al. 2010, *ApJ*, 721, 193
- Schlafly, E. F., & Finkbeiner, D. P. 2011, *ApJ*, 737, 103
- Sorba, R., & Sawicki, M. 2018, *MNRAS*, 476, 1532
- Stiavelli, M., Morishita, T., Chiaberge, M., et al. 2023, *ApJL*, 957, L18
- Strait, V., Brammer, G., Muzzin, A., et al. 2023, *ApJL*, 949, L23
- Topping, M. W., Stark, D. P., Endsley, R., et al. 2023, arXiv:2307.08835
- Treu, T., Schmidt, K. B., Brammer, G. B., et al. 2015, *ApJ*, 812, 114
- Trussler, J. A. A., Conselice, C. J., Adams, N., et al. 2024, *MNRAS*, 527, 11627
- Willott, C. J., Doyon, R., Albert, L., et al. 2022, *PASP*, 134, 025002
- Zheng, W., Postman, M., Zitrin, A., et al. 2012, *Natur*, 489, 406
- Zheng, W., Zitrin, A., Infante, L., et al. 2017, *ApJ*, 836, 210